Supporting Material: Structure-function relations and rigidity percolation in the shear properties of articular cartilage

Jesse L. Silverberg,[*] Aliyah R. Barrett,[†] Moumita Das,[‡]
Poul B. Petersen,[†] Lawrence J. Bonassar,[§] and Itai Cohen[*]

[*]Physics Department, Cornell University,
C10 Clark Hall, Ithaca, New York, 14853-1301

[†]Department of Chemistry and Chemical Biology, Cornell University,
122 Baker Laboratory, Ithaca, New York, 14853-1301

[§]School of Physics & Astronomy, Rochester Institute of Technology,
GOS 3338, Rochester, New York, 14623-5603

[‡]Biomedical Engineering, Mechanical and Aerospace Engineering, Cornell University,
149 Weill Hall, Ithaca, New York, 14853-1301

1 Nomenclature

For convenience, we include here a nomenclature of important terms and symbols used in the main text.

Terms

- AC - Articular Cartilage
- TDIS - Tissue Deformation Imaging Stage
- QPLM - Quantitative Polarized Light Microscopy
- FTIR-I - Fourier Transform Infrared Imaging
- PFG - Patellafemoral Groove
- TP - Tibial Plateau

Symbols

- z - The coordinate describing depth into an AC sample where $z = 0$ is the articular surface and increasing z moves toward the bone.
- $|G^*(z)|$ - The magnitude of the depth-dependent complex shear modulus.
- $\langle \mathrm{PI}(z) \rangle$ - The transversely averaged depth-dependent polarization index where $\langle \mathrm{PI}(z) \rangle = 0$ corresponds to a perfectly isotropic distribution of collagen fibers and $\langle \mathrm{PI}(z) \rangle = 1$ corresponds to perfectly aligned collagen fibers.
- $\langle \phi(z) \rangle$ - The transversely averaged depth-dependent fiber orientation where $\langle \phi(z) \rangle = 0^\circ \equiv 180^\circ$ is perpendicular to the articular surface and $\langle \phi(z) \rangle = 90^\circ$ is parallel to the articular surface.
- $v_a(z)$ - The depth-dependent aggrecan wet volume fraction.
- $v_c(z)$ - The depth-dependent collagen wet volume fraction.
- v_f - The fiber volume fraction used in the rigidity percolation model. Note: This quantity is spatially homogeneous and should be distinguished from $v_c(z)$, which is used to describe experimental data. In Fig. 6 of the main text, we use $v_c(z)$ in place of v_f to generate spatially heterogeneous depth-dependent lattices.
- p - The fraction of occupied bonds in the rigidity percolation model.
- ℓ_c - The bond length in the rigidity percolation model.

- α - The stretching modulus of fibers in the rigidity percolation simulation.

- κ - The bending modulus of fibers in the rigidity percolation simulation.

- μ_0 - The shear modulus of the reinforcing medium in the rigidity percolation simulation, which can be used to calculate the effective modulus experienced by a 1D fiber undergoing transverse displacements in the reinforcing medium μ.

2 Articular cartilage structure and extended comments on the compressive properties

A large body of literature exists on articular cartilage (AC) biochemistry and biomechanics. Here, we briefly summarize relevant portions of this literature, which though non-essential for our main arguments, provides a more detailed background of this field. Much of the content provided here can be found in a more detailed review[1].

The macroscopic mechanical properties of articular cartilage (AC) emerge from an multi-scale structural hierarchy with characteristic length scales set by tropocollagen molecules (length ≈ 300 nm), collagen fibrils ($1-10$ μm), collagen fibers ($0.1-1$ mm), and bulk tissue ($1-10$ mm). The orientation of collagen fibers are known to vary across the thickness of the tissue and can be broadly categorized into zones. While the specifics of this organization vary with animal, age, and location within the joint, the general schematic (Fig. 1, main text) is largely conserved. In addition to the collagen network, there also exists an interpenetrating proteoglycan network that consists of aggrecan molecules linked together through a backbone of hylauronic acid. This gel-like material carries a net negative electric charge and attracts water molecules into the collagen network. In turn, an osmotic pressure, which at physiological conditions ranges from 0.1 to 0.2 MPa, is generated that swells the collagen network, placing it in tension and providing a means to rigidify the otherwise floppy collagen network. Though the proteogycan network structure and content vary with age and disease, its physical interactions with the collagen network can be both electrostatic and mechanical. In the former, negative charge groups on the aggrecan interact with positive charge groups on collagen fibrils providing cohesion without forming covalent bonds. In the latter, there is evidence of frictional interactions between the collagen and proteoglycan networks.

Under externally applied axial tension, the mechanical properties are dominated by the collagen network, while under compression, the mechanics are dominated by the resistance of fluid flow through the porous collagen network. This particular feature is unique because many polymer systems couple the osmotic and tensile properties to the same microstructure. Indeed, these compressive properties of AC are well studied, and have been examined as function of depth, direction, collagen density, and fiber orientation[1, 2, 3, 4, 5, 6, 7, 8, 9, 10, 11, 12, 13, 14, 15]. Among this work, it has been observed the depth-dependent confined compression modulus of adult bovine PFG is a factor of 10 to 20 more compliant near the articular surface relative to the deep zone[13]. This point is important to note, as studies of random elastic networks have shown that a vanishing shear modulus, which arises due to reduced network connectivity, is associated with a vanishing bulk modulus[16]. Thus, evidence for this generic prediction of rigidity percolation is already present in the literature on AC's compressive properties, providing further support for the microscopic interpretation of the depth-dependent shear modulus put forth in the main text.

3 Experiment Schematics

In this work we employed three different experimental techniques to quantify mechanical and structural aspects of articular cartilage (AC) with high spatial resolution. As described in the main text, confocal elastography was used to study shear mechanical properties, QPLM was used to study collagen fiber organization, and FTIR-I was used to study matrix density. Here, we supplement descriptions of these techniques provided in the main text with schematic diagrams (Fig. 1).

4 Additional QPLM data

In the main text, we show the depth-dependent profile of the polarization index $\langle \mathrm{PI}(z) \rangle$ and fiber orientation $\langle \phi(z) \rangle$, along with error bars indicating ± 1 standard deviation arising from the average along the transverse direction. To provide a sense of sample-to-sample variation, we show here the depth-dependent measurements for all 8 samples (Fig. 2). Generally, we find in the tangential zone ($z < 100$ μm) that all samples have a high degree of collagen fiber alignment with $\langle \mathrm{PI} \rangle \gtrsim 0.5$ and $\langle \phi \rangle \approx 80°$, indicating the fibers are nearly parallel to the articular surface. For 100 $\mu\mathrm{m} < z < 400$ μm, the fiber alignment is much more random with $\langle \mathrm{PI} \rangle \approx 0.3 \pm 0.1$ and the average orientation $\langle \phi \rangle$ showing an overall decrease relative

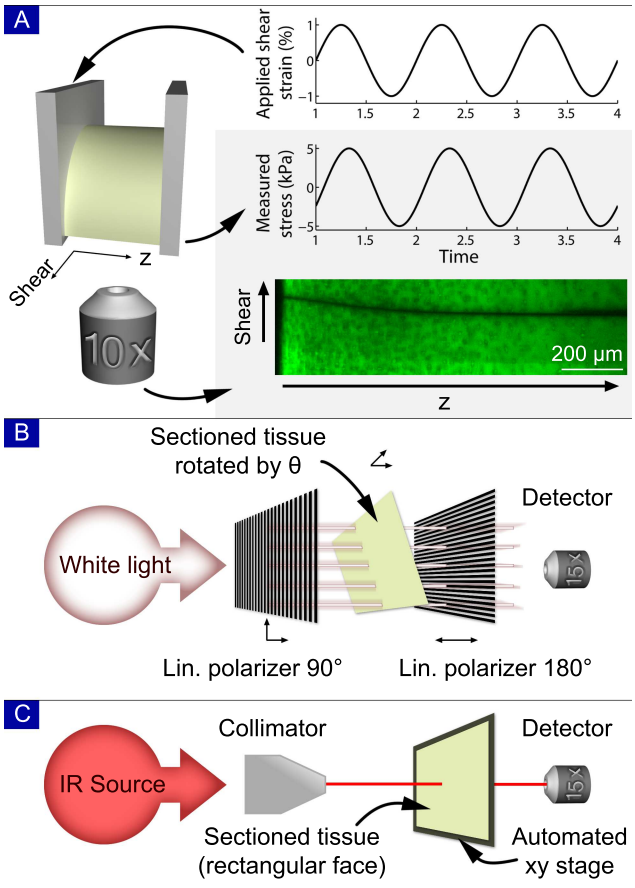

Figure 1: Schematic diagrams of the experimental methods used in this study including (A) confocal elastography, (B) quantitative polarized light microscopy, and (C) Fourier transform infrared imaging. Details are provided in the main text.

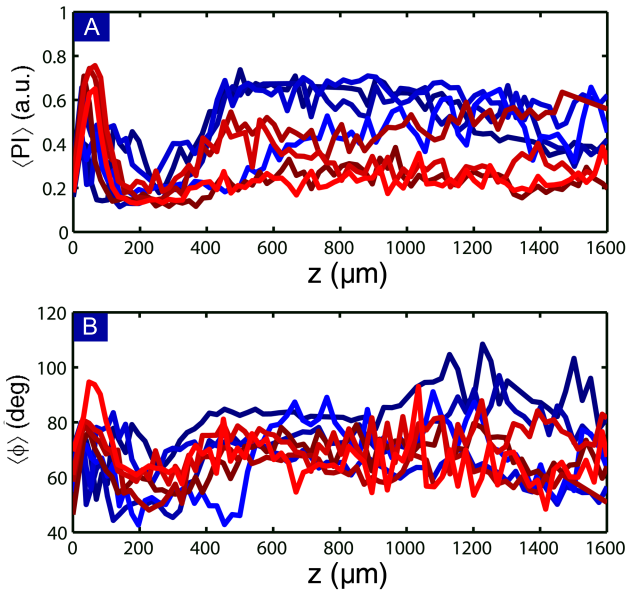

Figure 2: Data for every sample's (A) $\langle \mathrm{PI}(z) \rangle$ and (B) $\langle \phi(z) \rangle$ illustrating sample-to-sample variation. The region where $z < 100$ μm corresponds to the tangential zone. Red and blue coloring is coordinated to match Fig. 2 in the main text.

to the tangential zone. For $z > 400$ μm, there are notable regional differences in $\langle \mathrm{PI} \rangle$, though all samples show a tendency to increase to some mid-range value. For the average fiber orientation in this region, the mean value tends to be centered on $\langle \phi \rangle \approx 70°$, however, as shown in Fig. 3(B) in the main text, the standard deviation of $\langle \phi \rangle$ in this region is much higher than the region where $z < 100$ μm. Thus, when interpreting the mean fiber orientation, it must be realized that this data does not necessarily imply that the fibers are all aligned parallel to the articular surface. Rather, each depth-dependent measurement of $\langle \phi \rangle$ must be interpreted in context of the corresponding measurement of $\langle \mathrm{PI} \rangle$ to get a per-sample interpretation of how broadly distributed the collagen fiber orientation is about its mean angle.

In adult articular cartilage, the tangential, mid, and deep zones are generally identifiable by the mean fiber orientation (see Fig. 1 in main text). However, in immature tissue, this pattern of fiber alignment hasn't fully developed. Thus, in our samples, we only observe a clear tangential zone ($z < 100$ μm), with no clear distinction between the mid and deep zones. This is consistent with earlier QPLM studies on immature porcine AC that observed age-dependent differences in the collagen fiber architecture[17].

5 Depth-dependent matrix data

FTIR-I data was used to generate depth-dependent measurements of the collagen $v_c(z)$ and aggrecan $v_a(z)$ matrix volume fractions. In this analysis, the total AC spectra for each sample at each depth were decomposed into a linear combination of pure compound spectra and a baseline. The AC spectra are fit with the form:

$$\text{AC spectra} = c_1\times(\text{Pure type II collagen spectra}) + c_2\times(\text{Pure aggrecan spectra}) + [c_3\times(\text{wavenumber}) + c_4].$$

Here, $c_1 \propto v_c$ and $c_2 \propto v_a$, while c_3 and c_4 are coefficients that determine the baseline associated with instrument-specific deviations and drift. This approach, which is similar to a 2 component principle component analysis, minimizes the difference between the left and right hand sides by varying the 4 coefficients. The best fit values and their 95% confidence intervals are then used to determine matrix volume fractions. Though coarse in many respects, this approach to FTIR-I data analysis is sufficient for our purposes. Indeed, there are a variety of methods available for FTIR-I data analysis, and our results are consistent regardless of what method used (see summary Table 1)[18, 19, 20, 21, 22, 23, 24, 25, 26, 27, 5].

To illustrate that our main conclusion does not depend on the specific method of FTIR-I data analysis, we perform a naively coarse analysis of the absorbance spectra. While this is not the approach taken in the main text, it serves as an example of the robustness of the result that the shear modulus is strongly correlated with the matrix density. In this approach, we integrate the full IR spectra from 910 to 1726 cm^{-1} at each depth to determine the total amount of absorbance in the region of interest. According to Beer's law[28], this integrated absorbance serves as a measure proportional to solid matrix density. Plotting against the shear modulus in the same manner discussed in the main text again reveals a strong correlation (Fig. 3(A); $R = 0.85,\ p < 0.01$), and shows a 2-fold variation in matrix density is accompanied by a 100-fold variation in shear modulus. This method of analysis does not distinguish between collagen and aggrecan contributions, nor is it scaled to match experimentally measured volume fraction values. However, our argument in the main text that collagen fibers, and not the aggrecan matrix, are the most likely source for AC's depth-dependent shear properties remains valid.

As further demonstration of the main FTIR-I result's robustness, we use two additional methods of analysis commonly described in the literature and reproduce the observed correlations with $|G^*(z)|$. In the first method, we integrated the amide I peak from 1598 cm^{-1} to 1710 cm^{-1} and the carbohydrate peak between 950 cm^{-1} to 1150 cm^{-1} to quantify the collagen and aggrecan content, respectively (Fig. 3(B,C))[19, 20, 21, 22]. Numerical integration was performed for each spectrum at each depth and was scaled to the same bulk-averaged volume fraction as described in the main text. In the second method, we decomposed the spectra into a sum of Gaussian peaks centered on 1655 cm^{-1}, 1638 cm^{-1}, 1558 cm^{-1}, 1542 cm^{-1}, 1456 cm^{-1}, 1400 cm^{-1}, 1340 cm^{-1}, 1240 cm^{-1}, 1209 cm^{-1}, 1130 cm^{-1}, 1076 cm^{-1}, and 1036 cm^{-1}. Each wave number is either known to correlate with a biochemical bond specific to AC matrix content, or to a series of closely overlapped bonds, which again, have known correlates[23]. This approach allows adjacent peaks to be deconvolved and their individual collagen- or aggrecan-specific contribution to the absorbance quantified. In particular, the peak centered on 1655 cm^{-1} and 1036 cm^{-1} were used to measure collagen and aggrecan content, respectively (Fig. 3(D,E)). Both the peak integration method and Gaussian peak decomposition method agree favorably with the sum of spectra method that was used in the main text (scaled and reproduced in Fig. 3(F,G) for direct comparison). In the same vein, we fit each data set to the functional form $|G^*(v_c)| \sim (v_c - v_0)^\xi$. We found for the total integrated absorbance ξ ranged from 4.0 to 4.5, depending on the value of v_0. Similarly, for the collagen volume fraction quantified by peak integration ξ was between 2.1 and 5.9, while the collagen volume fraction quantified by Gaussian peak decomposition was between 2.1 and 6.1. Thus, all four approaches to FTIR-I data analysis lead to the conclusion that the exponent characterizing this structure-function relationship are anomalously high when compared to simple continuum materials.

In the analysis presented in the main text, the FTIR-I aggrecan spectrum acquired from literature was obtained from measurements of aggrecan extracted from bovine AC femoral condyles[23]. This spectrum, however, exhibits qualitative differences from that of purified calf nasal aggrecan, which has also been used to analyze cartilage matrix constituents[19]. Here, we perform the same correlation analysis on the FTIR-I data (Fig. 4(A,B)) using the latter aggrecan spectrum in place of the former (Fig. 4(C,D)), where again, the spectrum was acquired from published literature. We find the correlation between the aggrecan volume fraction v_a and shear modulus $|G^*|$ essentially disappears for $|G^*| > 0.2$ MPa, while the correlation with collagen is largely unchanged for all v_c. Indeed, the power-law fits (Fig. 4(D), lines) are entirely consistent regardless of which aggrecan spectrum is used. This can be understood as arising from the relatively small amount of aggrecan in the matrix, which is typically $\approx 25\%$ of the overall solid content (Fig. 5(B)), and the general coarseness of decomposing each spectrum into the sum of col-

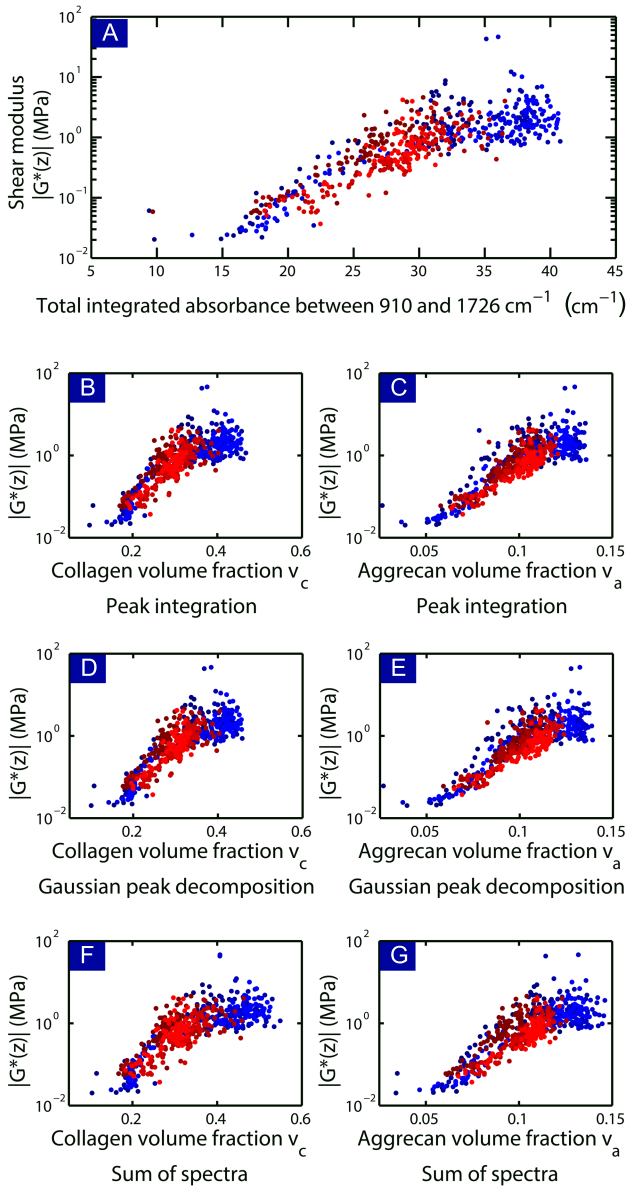

Figure 3: Four different methods to analyze FTIR-I data all produce the same correlation between matrix content and shear modulus. Plotting same-sample measurements of the depth-dependent shear modulus against (A) the total integrated absorbance, (B) the integrated Amide I peak, (C) the integrated carbohydrate peak, (D) Gaussian decomposition of the Amide I peak, (E) Gaussian decomposition of the carbohydrate peak, (F) collagen contribution of a 2 component spectral sum, and (G) aggrecan contribution of a 2 component spectral sum all lead to self-consistent results. Red and blue coloring is coordinated to match Fig. 2 in the main text.

Method	ξ
Total integrated area	4.0 - 4.5
Peak integration	2.1 - 5.9
Gaussian peak decomposition	2.1 - 6.1
Sum of spectra (Rieppo data[23])	1.7 - 4.5
Sum of spectra (Camacho data[19])	2.4 - 4.7

Table 1: Summary of best-fit power law exponent ξ from FTIR-I analysis for collagen volume fraction data. For entry using the total integrated area method, volume fractions represent total solid matrix content, not just collagen content.

lagen and aggrecan. Thus, we find the data leads to the same conclusion regarding anomalous scaling between $|G^*|$ and v_c, independent of the aggrecan spectrum's source.

In the main text only one specific depth-dependent FTIR-I measurement was shown. Here, we present all measurements (Fig. 5(A)). One possible source for spatial variations in matrix volume fraction are artifacts arising from sample preparation; if tissue samples were sectioned in a manner that caused spatial variations in thickness, we would find an enhanced absorbance and consequently a spatial variation in the matrix concentration. Since the in-plane sample orientation was random during the sectioning process, all sectioning cuts were made from different directions. Thus, we can check for this possible artifact by examining the ratio of $v_a(z)/v_c(z)$ (Fig. 5(B)). For each sample, we find a consistent depth-dependent profile where the surface region ($z < 200$ μm) has an overall increase relative to deeper tissue. This trend can be made more explicit by normalizing the ratio $v_a(z)/v_c(z)$ by each contour's average value for $z > 600$ μm (Fig. 5(C)). If sectioning artifacts were present, we would expect random deviations from the overall trend, however, within noise, we observe a consistent behavior for all samples indicating variations in tissue thickness do not drive the depth-dependent variations in $v_a(z)$ and $v_(z)$.

6 Phenomenological fits

From a phenomenological continuum mechanics perspective, we quantified the relation between matrix concentration and shear modulus by fitting $v_a(z)$ and $v_c(z)$ to $|G^*(z)|$ with the expressions $A_a[v_a(z)]^{p_a}$ and $A_c[v_c(z)]^{p_c}$. In Fig. 6 we show an example best fit for sample PFG 1, as well as the aggregate results for all 8 samples. Consistent with the power-law nature of these expressions and scatter in the data, the exponents p_a and p_c were found to have relatively small 95% confidence intervals, while the coefficients A_a and A_c did not. Averaging the expo-

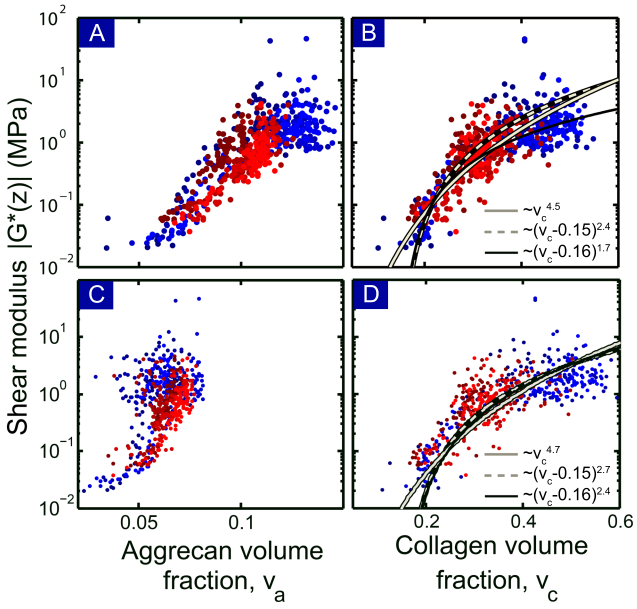

Figure 4: Comparison of shear modulus and matrix volume fraction correlations when using a purified bovine nasal aggrecan spectrum instead of a bovine femoral condyle aggrecan spectrum. (A,B) Correlation plots from main text Fig. 4 are reproduced for easy comparison. (C,D) Correlation plots using a bovine nasal aggrecan spectrum show a lack of correlation with v_a for $|G^*| > 0.2$ MPa, and a nearly identical correlation with v_c when compared to the numerical values of the fits presented in (B).

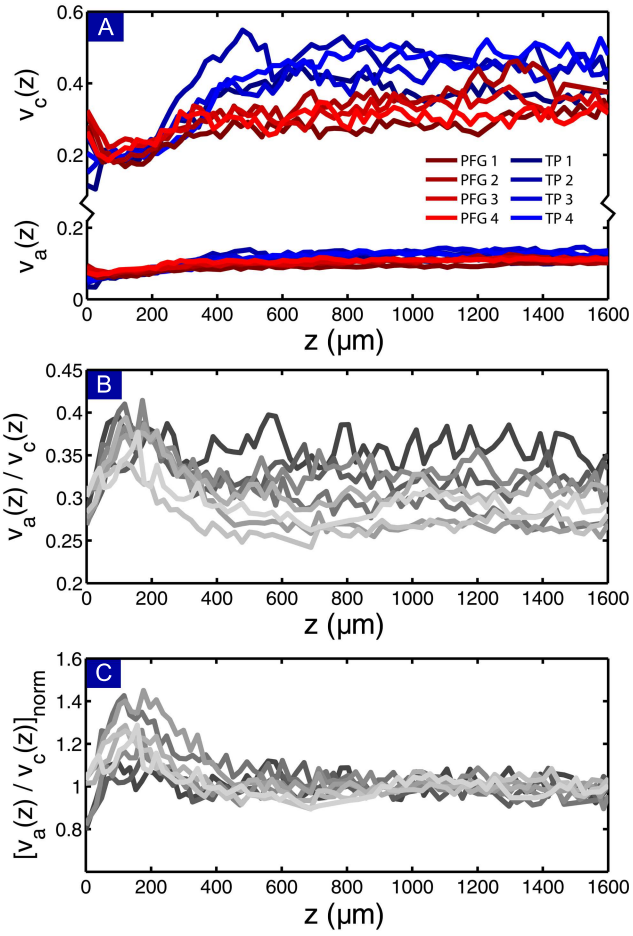

Figure 5: (A) We show the depth-dependent aggrecan and collagen volume fractions $v_a(z)$ and $v_c(z)$ for all 8 samples. Note the break in the vertical scale. Red and blue coloring is coordinated to match Fig. 2 in the main text. (B) The ratio of $v_a(z)/v_c(z)$ is plotted as a function of depth to investigate the possibility that depth-dependent variations in matrix volume fraction arise from sample preparation artifacts. (C) Normalizing each $v_a(z)/v_c(z)$ curve by its average value for $z > 600$ μm collapses the curves on to a single master curve that, within noise, is consistent across all samples. This indicates sectioning artifacts are not present in the system.

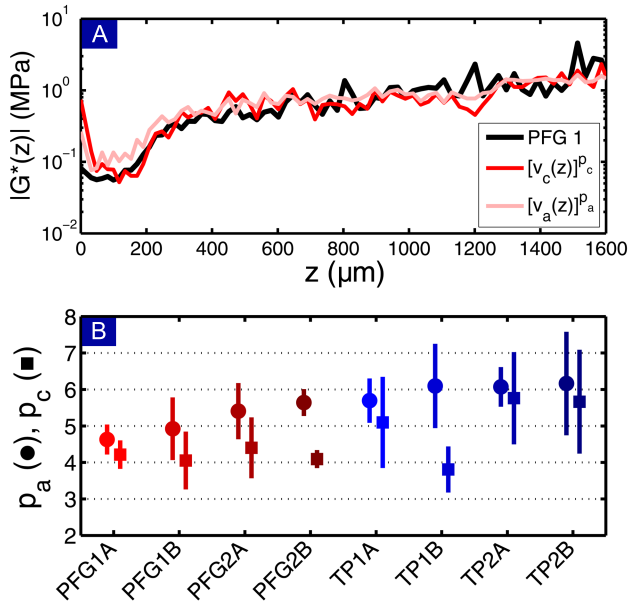

Figure 6: (A) Phenomenologically fitting $v_a(z)$ and $v_c(z)$ to $|G^*(z)|$ via a power law results in reasonable agreement between the different data sets, as illustrated here with sample PFG 1. (B) Across all 8 samples, the power law exponents p_a and p_c are found to fall within a limited range, suggesting an anomalously large scaling between the matrix concentration and shear modulus. Red and blue coloring is coordinated to match Fig. 2 in the main text.

nents, we find $\bar{p}_a = 5.6 \pm 0.5$ and $\bar{p}_c = 4.6 \pm 0.8$, both of which are anomalously larger than the typical constitutive relationships used to describe homogeneous media. Note that this method is distinct from what was described in the main text where fitting between shear modulus and collagen volume fraction was performed on all 8 samples aggregated together, whereas this is on a per-sample basis.

7 Residual analysis of fits

With MATLAB's standard fitting algorithms there is a requirement that the fitting function evaluated over the full domain produces real numbers. However, scatter in experimental data produces data points at v_c lower then values of v_0 that we would reasonably fit for. Consequently, the algorithm evaluates negative numbers raised to non-integer exponents, causing terminal errors. We addressed this issue by inverting the fitting function from $|G^*| = A(v_c - v_0)^\xi$ to $v_c = v_0 + (|G^*|/A)^{1/\xi}$. Though a subtle shift in what is typically a straight-forward procedure, this step is necessary in order to make use of all

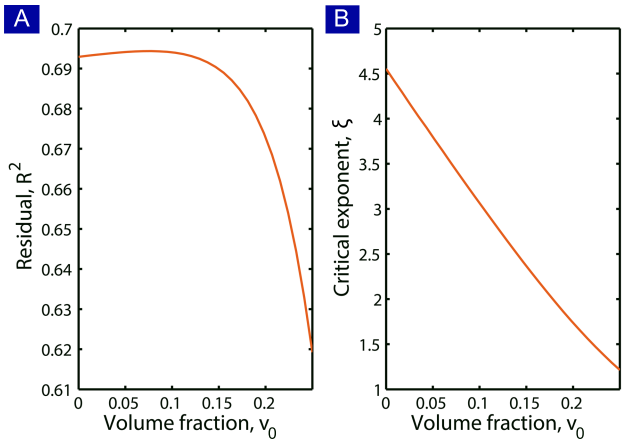

Figure 7: (A) The fitting residual R^2 is a measure of how much data variance can be attributed to a particular functional form. For the scaling function used here, we found a range of values for v_0 gave comparable results. (B) The critical exponent ξ associated with a given v_0 varied strongly over a factor of 3.

available data and not just the points where $v_c > v_0$.

As described in the main text, we found an expression of the form $|G^*| \sim (v_c - v_0)^\xi$ had fits of nearly indistinguishable quality over a range of v_0 from 0.0 to 0.15. In Fig. 7 we show the full results of the residual analysis. We find there is a weak maximum at $v_0 \approx 0.07$ but that given the context of how weakly R^2 varies with v_c, this "best fit" can't be used to justify the exponent $\xi = 3.4$ over any other exponent in the range of 2.4 to 4.5.

8 Loading-condition dependence of model

Because mechanical response depends on loading conditions, we explored the depth-wise compression and shear amplitude dependence of the reinforced fiber network. At 0%, 1%, and 7% compression with a fixed 1% shear amplitude, we found a decrease in the modulus with increasing compression (Fig. 8(A)). This behavior is consistent with previous experiments[29], and arises from a shear strain induced relaxation of fiber bending caused by the applied compression. Applying 1%, 4%, and 7% simple shear with 0% compression, we found $G(v_f)$ is insensitive to shear amplitude (Fig. 8(B)). This is because the energy density in the linear elastic approximation scales as the strain squared, while $G(v_f)$ in the same approximation scales as the energy density divided by strain squared[30]. Experiments however, show a shear stiffening response as

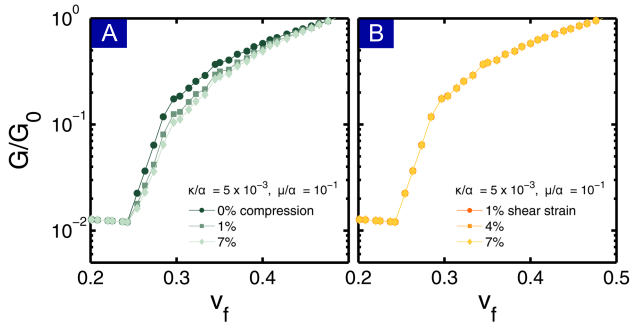

Figure 8: To understand the percolating fiber networks loading-condition dependence, we varied (A) the axial compression at fixed shear strain, and (B) the shear strain amplitude at fixed compression. The model exhibits a compression-induced softening in the shear modulus, but is independent of the strain amplitude.

the shear amplitude increases[29]. Evidently, higher-order terms must be included in the energy expression to account for all the loading condition dependent behavior.

Supporting References

[1] V. C. Mow, A. Ratcliffe, and A. R. Poole. Cartilage and diarthrodial joints as paradigms for hierarchical materials and structures. *Biomaterials*, 13:67–97, 1992.

[2] S Cowin and S Doty. *Tissue Mechanics*. Springer Science, New York, 1 edition, 2007.

[3] P. Julkunen, P. Kiviranta, W. Wilson, J. S. Jurvelin, and R. K. Korhonen. Characterization of articular cartilage by combining microscopic analysis with a fibril-reinforced finite-element model. *J. Biomech.*, 40:1862–1870, 2007.

[4] P. Julkunen, W. Wilson, J. S. Jurvelin, J. Rieppo, C.-J. Qu, M. J. Lammi, and R. K. Korhonen. Stress relaxation of human patellar articular cartilage in unconfined compression: Prediction of mechanical response by tissue composition and structure. *J. Biomech.*, 44:1978–1986, 2008.

[5] L. Rieppo, S. Saarakkala, J. S. Jurvelin, and J. Rieppo. Prediction of compressive stiffness of articular cartilage using Fourier transform infrared spectroscopy. *J. Biomech.*, 44:1269–1275, 2013.

[6] L. P. Rasanen, M. E. Mononen, M. T. Nieminen, E. Lammentausta, J. S. Jurvelin, R. K. Korhonen, and OAI-Investigators. Implementation of subject-specific collagen architecture of cartilage into a 2D computational model of a knee joint – Data from the Osteoarthritis Initiative (OAI). *J. Orthop. Res.*, 31: 10–22, 2013.

[7] K. S. Halonen, M. E. Mononen, J. S. Jurvelin, J. Toyras, and R. K. Korhonen. Importance of depth-wise distribution of collagen and proteoglycans in articular cartilage – A 3D finite element study of stresses and strains in human knee joint. *J. Biomech.*, 46:1184–1192, 2013.

[8] V. C. Mow, S. C. Kuei, W. M. Lai, and C. G. Armstrong. Biphasic creep and stress relaxation of articular cartilage in compression: Theory and experiments. *J. Biomech. Eng.*, 102:73–84, 1980.

[9] V. C. Mow, M. H. Holmes, and W. M. Lai. Fluid transport and mechanical properties of articular cartilage: A review. *J. Biomech.*, 17:377–394, 1984.

[10] W. M. Lai, J. S. Hou, and V. C. Mow. A triphasic theory for the swelling and deformation behaviors of articular cartilage. *J. Biomech. Eng.*, 113:245–258, 1991.

[11] A. K. Williamson, A. C. Chen, and R. L. Sah. Compressive properties and function-composition relationships of developing bovine articular cartilage. *J. Orthop. Res.*, 19:1113–1121, 2001.

[12] R. M. Schinagl, M. K. Ting, J. H. Price, and R. L. Sah. Video microscopy to quantitative the inhomogeneous equilibrium strain within articular cartilage during confined compression. *Ann. Biomed. Eng.*, 24: 500–512, 1996.

[13] R. M. Schinagl, D. Gurskis, A. C. Chen, and R. L. Sah. Depth-dependent confined compression modulus of full-thickness bovine articular cartilage. *J. Ortho. Res.*, 15:499–506, 1997.

[14] N. O. Chahine, C. C. Wang, and C. T. Hung. Anisotropic strain-dependent properties of bovine articular cartilage in the transitional range from tension to compression. *J. Biomech.*, 37:1251–1261, 2004.

[15] J. H. Lai and M. E. Levenston. Meniscus and cartilage exhibit distinct intra-tissue strain distributions under unconfined compression. *Osteoarthritis Cartilage*, 18: 1291–1299, 2010.

[16] W. G. Ellenbroek, Z. Zeravcic, W. van Saarloos, and M. van Hecke. Non-affine response: Jammed packings vs. spring networks. *EPL*, 87:34004–1, 2009.

[17] J. Rieppo, J. Hallikainen, J. Jurvelin, I. Kiviranta, H. J. Helminen, and M. M. Hyttinen. Practical considerations in the use of polarized light microscopy in the analysis of the collagen network in articular cartilage. *Microsc. Res. Techniq.*, 71:279–287, 2008.

[18] L. Rieppo, J. Rieppo, J. S. Jurvelin, and S. Saarakkala. Fourier transform infrared spectroscopic imaging and multivariate regression for prediction of proteoglycan content of articular cartilage. *PLoS ONE*, 7:1–8, 2012.

[19] N. P. Camacho, P. West, P. A. Torzilli, and R. Mendelsohn. FTIR microscopic imaging of collagen and proteoglycan in bovine cartilage. *Biopolymers*, 62:1–8, 2001.

[20] X. Bi, G. Li, S. B. Doty, and N. P. Camacho. A novel method for determination of collagen orientation in cartilage by Fourier transform infrared imaging spectroscopy FT-IRIS. *Osteoarthr. Cartilage*, 13: 1050–1058, 2005.

[21] X. Bi, X. Yang, M. P. G. Bostrom, and N. P. Camacho. Fourier transform infrared imaging spectroscopy investigation in the pathogenesis and repair of cartilage. *Biochim. Biophys. Acta*, 1758:934–941, 2006.

[22] Y. Xia, N. Ramakrishnan, and A. Bidthanapally. The depth-dependent anisotropy of articular cartilage by Fourier-transform infrared imaging (FTIR). *Osteoarthr. Cartilage*, 15:780–788, 2007.

[23] L. Rieppo, S. Saarakkala, T. Narhi, J. Holopainen, M. Lammi, H. J. Helminen, J. S. Jurvelin, and J. Rieppo. Quantitative analysis of spatial proteoglycan content in articular cartilage with Fourier transform infrared imaging spectroscopy: Critical evaluation of analysis methods and specificity of the parameters. *Microsc. Res. Techniq.*, 73:503–512, 2010.

[24] J. Yin and Y. Xia. Macromolecular concentrations in bovine nasal cartilage by Fourier transform infrared imaging and principle component regression. *Appl. Spectrosc.*, 64:1199–1208, 2010.

[25] J. Yin, Y. Xia, and M. Lu. Concentration profiles of collagen and proteoglycan in articular cartilage by Fourier transform infrared imaging and principal component regression. *Spectrochim Acta A-M*, 88:90–96, 2012.

[26] Y. Xia, D. Mittelstaedt, N. Ramakrishnan, M. Szarko, and A. Bidthanapally. Depth-dependent anisotropies of amides and sugar in perpendicular and parallel sections of articular cartilage by Fourier transform infrared imaging. *Microsc. Res. Techniq.*, 74:122–132, 2011.

[27] Y. Xia, H. Alhadlaq, N. Ramakrishnan, A. Bidthanapally, F. Badar, and M. Lu. Molecular and morphological adaptations in compressed articular cartilage by polarized light microscopy and Fourier-transform infrared imaging. *J. Struct. Biol.*, 164:88–95, 2008.

[28] Brian Smith. *Fundamentals of Fourier Transform Infrared Spectroscopy*. CRC Press, Boca Raton, 1 edition, 2006.

[29] M. R. Buckley, A. J. Bergou, J. Fouchard, L. J. Bonassar, and I. Cohen. High-resolution spatial mapping of shear properties in cartilage. *J. Biomech.*, 43: 796–800, 2010.

[30] D. A. Head, A. J. Levine, and F. C. MacKintosh. Deformation of cross-linked semiflexible polymer networks. *Phys. Rev. Lett.*, 91:108102–1, 2003.